Dynamically Encircling Exceptional Points in Different Riemann Sheets for Orbital Angular Momentum Topological Charge Conversion

Huixin Qi,[1] Yandong Li,[1] Xiaoxiao Wang,[1,2] Yaolong Li,[1] Xuyang Li,[1] Xingyuan Wang,[6,*] Xiaoyong Hu,[1,2,3,4,5,†] and Qihuang Gong[1,2,3,4,5]

[1]*State Key Laboratory for Mesoscopic Physics and Department of Physics, Collaborative Innovation Center of Quantum Matter and Frontiers Science Center for Nano-optoelectronics, Peking University, Beijing 100871, China*

[2]*Beijing Academy of Quantum Information Sciences, Beijing 100193, China*

[3]*Peking University Yangtze Delta Institute of Optoelectronics, Nantong, Jiangsu 226010, China*

[4]*Collaborative Innovation Center of Extreme Optics, Shanxi University, Taiyuan, Shanxi 030006, China*

[5]*Hefei National Laboratory, Hefei 230088, China*

[6]*College of Mathematics and Physics, Beijing University of Chemical Technology, Beijing 100029, China*

(Received 18 November 2023; accepted 17 May 2024; published 14 June 2024)

Orbital angular momentum (OAM) provides an additional degree of freedom for optical communication systems, and manipulating on-chip OAM is important in integrated photonics. However, there is no effective method to realize OAM topological charge conversion on chip. In this Letter, we propose a way to convert OAM by encircling two groups of exceptional points in different Riemann sheets. In our framework, any OAM conversion can be achieved on demand just by manipulating adiabatic and nonadiabatic evolution of modes in two on-chip waveguides. More importantly, the chiral OAM conversion is realized, which is of great significance since the path direction can determine the final topological charge order. Our Letter presents a special chiral behavior and provides a new method to manipulate OAM on the chip.

DOI: 10.1103/PhysRevLett.132.243802

Introduction.—Orbital angular momentum (OAM) introduces an additional degree of freedom for optical communication systems [1]. It is characterized by a spiral phase front of $\exp(-il\theta)$, where l is the topological charge and θ is the azimuthal angle. Theoretically, it can form infinite Hilbert space with different l [2]. OAM conversion is necessary so that more complex information processing can be realized through multichannel information exchange. The most applicable platform for manipulating OAM is metasurface [3,4]. By particularly designing the parameters of the metasurface, it is achievable to convert different OAM modes in free space [5–7]. Another straightforward approach for OAM conversion involves employing helical phase plates, which comprise optical elements with helical phase delays [8]. Similarly, specific phase modulation techniques can be implemented using liquid crystal elements for OAM conversion [9,10]. Furthermore, on-chip OAM conversion is important in integrated photonics. By developing efficient and compact devices for manipulating OAM [11,12], it can be integrated with other on-chip optical devices for a wide range of applications. In recent years, laser direct writing has emerged as a promising platform for on-chip OAM transmission [13,14]. However, achieving efficient conversion of OAM topological charges on chip remains a pressing challenge.

When two or more eigenvalues and their corresponding eigenvectors in the parameter space of the system degenerate, singularities will generate that are known as exceptional points (EPs) [15–17], which are special in non-Hermitian systems [18–20]. A sufficiently slow change of system parameters near EPs [21–27] can be used as an effective means of on-chip information processing and control, and the conversion of optical degrees of freedom occurs in a variety of systems [28,29], such as asymmetric modes conversion [30,31], polarization states conversion [32], quantum states conversion, etc. Table I compares our Letter with Refs. [31–33].

In this Letter, we propose a method to realize the conversion of OAM modes with different topological charges by encircling EPs in different Riemann sheets. We construct a non-Hermitian system consisting of two doughnut-shaped waveguides. When different orders of OAM in one waveguide couple with the same order of OAM in the other waveguide, it leads to the generation of two distinct sets of Riemann sheets. The chiral behavior is of great importance since it can be used for OAM mode conversion. For clockwise (CW) loop, topological charge changes from higher to lower. For counterclockwise (CCW) loop, it changes from lower to higher. Our Letter presents a special chiral behavior and provides a new

method to manipulate OAM for on-chip photonic techniques.

We consider two coupled waveguides systems (WG-a with OAM eigenmodes of topological charge $l = \pm 1$ or $l = \pm 2$ and WG-b with $l = \pm 1$). Refractive indexes of WG-b are different in two cases [34–36]. Hamiltonian $H(t)$ at certain time t takes the form of Eq. (1), which is governed by $i\partial_t|\psi(t)\rangle = H(t)|\psi(t)\rangle$. Generally, modes in a waveguide are orthogonal [37–39]. $H(t)$ is derived from coupled-mode theory for weakly guiding modes [40–42] (detailed in Supplemental Material, Sec. I [43]),

$$H(t) = \begin{bmatrix} \beta_{l=1}^{(b)} & \kappa_{l=1,l=1} & \kappa_{l=1,l=2} \\ \kappa_{l=1,l=1} & \beta_{l=1}^{(a)}(t) - i\gamma(t) & 0 \\ \kappa_{l=1,l=2} & 0 & \beta_{l=2}^{(a)}(t) - i\gamma(t) \end{bmatrix}, \quad (1)$$

where each element is a 4×4 matrix because one single waveguide supports four OAM eigenmodes with $\pm l$ and two vertical polarizations. The diagonal elements β represent the propagation constant of OAM modes [44]. The subscripts $l = 1$, $l = 2$ represent the topological charge of OAM modes supported by WG-a and WG-b (superscripts). κ represents the coupling coefficient of modes between WG-a and WG-b [45,46]. γ is the loss of WG-b. (The relationship between β, γ and the refractive index n, k is detailed in Supplemental Material, Sec. I. [43]) We obtain the eigenvalues by solving Eq. (1). Figure 1(a) is the real part of the eigenvalues. There are two groups of EPs (EP1 and EP2 in red box) in Space-1 and Space-2. Space-1 is the Riemann sheets formed by the coupled OAM modes with $l = \pm 1$ in WG-a and $l = \pm 1$ in WG-b, which contains four EPs (red points marked by 1,2,3,4), as shown in Fig. 1(b). Space-2 is formed by the coupled OAM modes of $l = \pm 2$ in WG-a and $l = \pm 1$ in WG-b with four EPs (red points marked by 1', 2', 3', 4'), as shown in Fig. 1(c). The high-loss Riemann sheets of Space-1 and Space-2 are connected by one group of EPs [EP-12 in Fig. 1(a)], which is formed by the coupled OAM modes of $l = \pm 1$ and $l = \pm 2$ in WG-a. The low-loss Riemann sheets of Space-1 and Space-2 share the same Riemann sheets. Figure 1(d) is the imaginary parts of the eigenvalues; two groups of EPs are marked by 1,2,3,4 and 1', 2', 3', 4'.

We consider a rectangular loop in Eq. (2a) and Eq. (2b) with the initial point and end point at $t_0 = 0$ and $t_5 = T$, respectively. T is the encircling period and $t_i = i \cdot (T/5)$,

$$\beta(t) = \begin{cases} \rho_0 + \frac{\alpha\rho(t-t_0)}{t_1-t_0} & t_0 \le t \le t_1 \\ \rho_0 + \alpha\rho t_1 & t_1 < t \le t_2 \\ \rho_0 + \alpha\left(\rho - \frac{3\rho(t-t_2)}{t_3-t_2}\right) & t_2 < t \le t_3 \\ \rho_0 + 2\alpha\rho t_3 & t_3 < t \le t_4 \\ \rho_0 + \alpha\left(2\rho + \frac{2\rho(t-t_4)}{t_5-t_4}\right) & t_4 < t \le t_5 \end{cases}, \quad (2a)$$

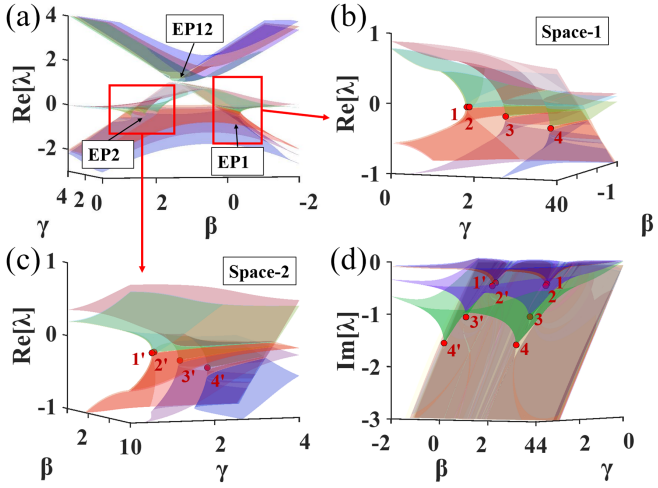

FIG. 1. (a) Real part of eigenvalues as a function of γ and β. It contains two groups of EPs (EP1 and EP2) (b) Space-1. The red points 1, 2, 3, 4 are four EPs of EP-1. (c) Space-2. The red points 1', 2', 3', 4' are four EPs of EP-2. (d) Imaginary part of eigenvalues.

$$\gamma(t) = \begin{cases} \rho_1 - \rho t_0 \le t \le t_1 \\ \rho_1 - \rho + \frac{2\rho(t-t_1)}{t_2-t_1} t_1 < t \le t_2 \\ \rho_1 + \rho t_2 < t \le t_3 \\ \rho_1 + \rho - \frac{2\rho(t-t_1)}{t_2-t_1} t_3 < t \le t_4 \\ \rho_1 - \rho t_4 < t \le t_5 \end{cases}, \quad (2b)$$

where $(\rho_0, 0)$ is the start coordinate of the encircling path and ρ is path radius. $\rho_0 = 0$ and $\rho_0 = \rho$ represent the initial point that lies at Space-1 and Space-2, whose eigenstates are $|\psi_{A1}\rangle, |\psi_{B1}\rangle, |\psi_{C1}\rangle$ and $|\psi_{A2}\rangle, |\psi_{B2}\rangle, |\psi_{C2}\rangle$, respectively. The loop is CCW when $\alpha < 0$ and CW when $\alpha > 0$. We solve time-dependent equation numerically and extract the amplitudes of instantaneous eigenstates at each time step [21], i.e.,

$$|\psi(t)\rangle = \sum_{i=1}^{3} C_i |\psi_i(t)\rangle, \quad (3)$$

where subscripts are associated with the eigenstates on different sheets. In the same space, encircling an EP has the same phenomenon as encircling a group of EPs, demonstrated in Supplemental Material, Sec. II [43]. Therefore, to simplify the model, we employ analysis with three eigenstates. We obtain the trajectories of the state evolution (blue curves) on the Riemann sheets [21] and the corresponding amplitude coefficients $\log(C_i)$. The initial and end states are marked by the blue and yellow points, respectively. We consider a loop ($\alpha < 0$, $\rho = 2$, $\rho_0 = 1$, $\rho_1 = 1.5$) in Figs. 2(a) and 2(b). For CW loop starting at $|\psi_{A1}\rangle$, the state first evolves adiabatically in Space-1. A nonadiabatic transition (NAT) occurs after a certain time, leading the

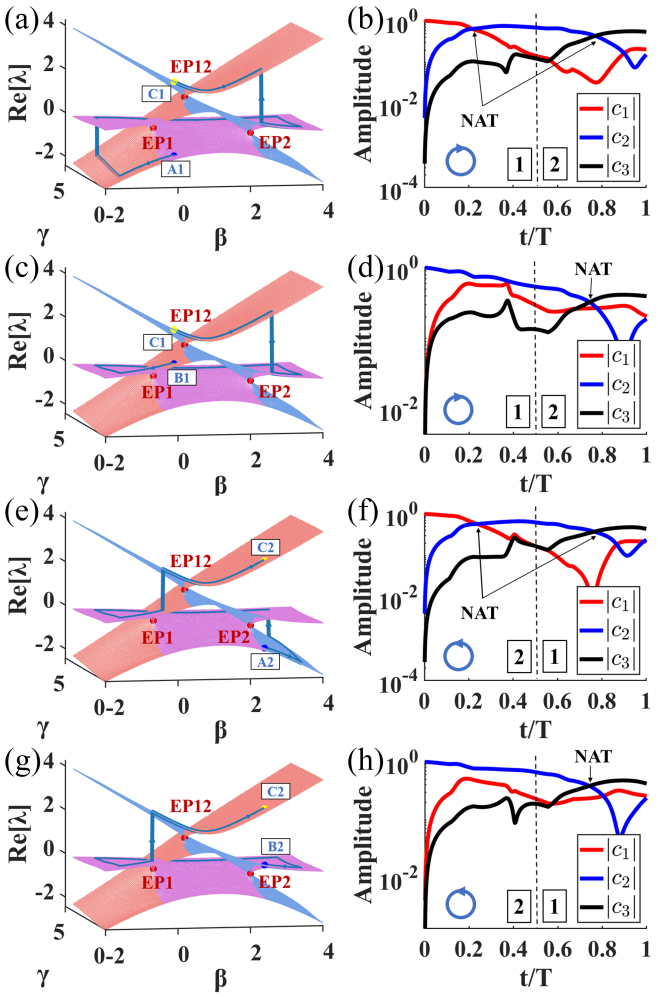

FIG. 2. OAM conversion behavior by dynamically encircling EPs in different Riemann sheets. (a),(c),(e),(g) Three-dimensional trajectory (blue curves) in the real part of the eigenvalues with different encircling directions and initial states. The blue and yellow points are the starting and end points. (b),(d),(f),(h) Calculated amplitudes of eigenstates.

state to evolve on the low-loss Riemann sheet (purple) that connects the two spaces. Then the state evolves adiabatically from Space-1 to Space-2. Finally, the state experiences a NAT in Space-2 and evolves to $|\psi_{C1}\rangle$. While starting at state $|\psi_{B1}\rangle$, as illustrated in Figs. 2(c) and 2(d), the state evolves adiabatically on the low-loss Riemann sheet (purple) from Space-1 to Space-2. Finally, the state experiences a NAT in Space-2 and evolves to $|\psi_{C1}\rangle$. For such process, we realize conversion of OAM from $l = 1$ to $l = 2$.

We then consider a loop ($\alpha > 0$, $\rho = 1$, $\rho_0 = 0$, $\rho_1 = 1.5$). As shown in Figs. 2(e) and 2(f), for CCW loop starting at state $|\psi_{A2}\rangle$, the state first evolves adiabatically in Space-2. NAT occurs after a certain time. Then the state evolves adiabatically from Space-2 to Space-1. Finally, the state experiences a NAT in Space-1 and evolves to $|\psi_{C2}\rangle$. While starting at state $|\psi_{B2}\rangle$, as illustrated in Figs. 2(g) and 2(h), the state evolves adiabatically from Space-2 to Space-1. Finally, the state experiences a NAT in Space-1 and evolves to $|\psi_{C2}\rangle$. For such process, we achieve conversion of OAM from $l = 2$ to $l = 1$. No conversion occurs in the opposite encircling direction (detailed in Supplemental Material, Sec. III [43]).

We then demonstrate the evolution of the Hamiltonian with time t by using the waveguide transmission process along the z direction. Because the coupled-mode theory equation is mathematically equivalent to a time-dependent Schrödinger's equation, time parameter t can be linearly mapped onto propagation axis z (detailed in Supplemental Material, Sec. I [43]). We construct a practical waveguide system for on-chip OAM conversion with two coupled doughnut-shape waveguides [WG-1 and WG-2 of inset in Fig. 3(a)]. The background refractive index is 1.44. The refractive index of WG-1 and WG-2 is $n_0 + \Delta n(z) + i\Delta k(z)$ and $n_0 (n_0 = 1.442)$. $n(z) = n_0 + \Delta n(z)$ and $k(z) = \Delta k(z)$ are the real and imaginary refractive index of WG-1 as a function of z. We only change the parameters of WG-1 to induce the coupling of modes carrying different OAM in WG-1 through WG-2, since these modes are orthogonal and have no coupling effect. For doughnut-shape waveguides with identical parameters, the topological charge of OAM eigenmodes increases as n increases, because higher-order OAM modes have a smaller effective mode index (n_{eff}) than lower-order modes. We calculate the n_{eff}, i.e., the eigenvalue of the waveguide system, as a function of $n(z)$ and $k(z)$. The real parts of the eigenvalues are shown in Fig. 3(a), which form two groups of EPs (EP1 and EP2 marked with red points). Giving specific waveguide parameters $\Delta n = -10^{-3}$ and $\Delta k = 4 \times 10^{-5}$, mode $l = \pm 1$ in WG-1 is coupled to $l = \pm 1$ in WG-2. We choose these two eigenstates (A1 and B1, marked with blue points) as the initial states of the CW process. When $\Delta n = 0$, the mode $l = \pm 2$ in WG-1 is coupled to $l = \pm 1$ in WG-2 (A2 and B2 as the initial states of the CCW process). The eigenfield and phase distributions of eigenstates $A1, B1, A2, B2$ are shown in Fig. 3(b).

The configuration is shown in Fig. 3(c). Along z direction, we vary the parameters of WG-1 as a function of n and k, the loop functions are detailed in Eq. S(20) and Eq. S(21) in Supplemental Material, Sec. III [43], as shown in Figs. 3(d) and 3(e). The initial states are A1 or B1 for CW process (Loop1) and A2 or B2 for CCW process (Loop2). The total length of the system is 10 mm, which is long enough to ensure adiabatic evolution. Simulation results are calculated through LUMERICAL FDTD solutions. We show the xz transmission field intensity distributions of the evolution (middle in Fig. 4) and the xy phase distributions of the input and output states (bottom and top in Fig. 4).

For Loop1 with eigenstate $A1$ input at $z = 0$ (Fig. 4(a)), the topological charge in WG-1 is $l = 1$. When $0 < z < L/2$, the state evolves in Space-1. During this

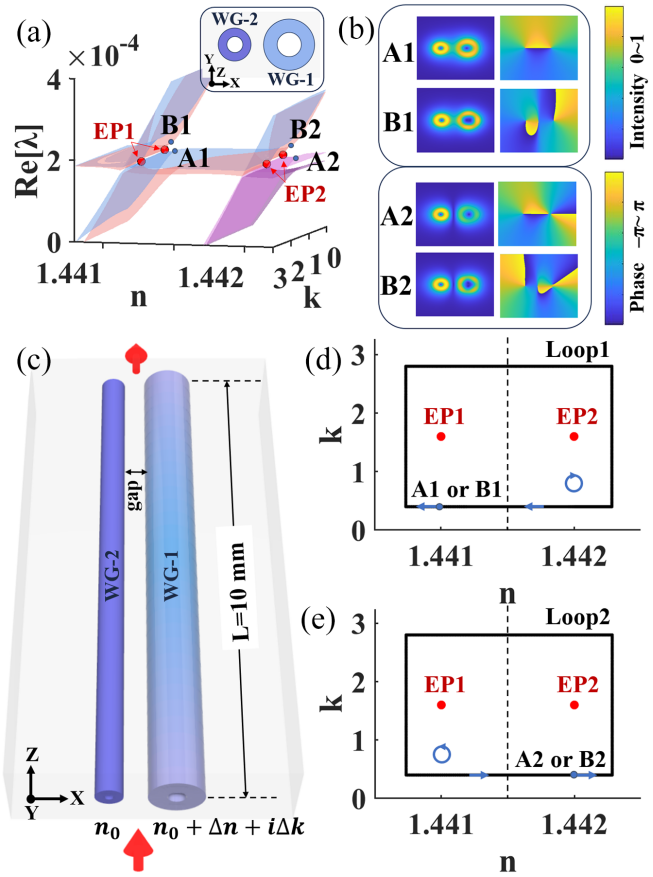

FIG. 3. (a) Real part of the n_{eff} of the system as a function of n and k. (b) Eigenstates of $A1, B1, A2, B2$. (c) System configuration. (d),(e) Loop-1 and Loop-2 of the practical system as a function of n and k.

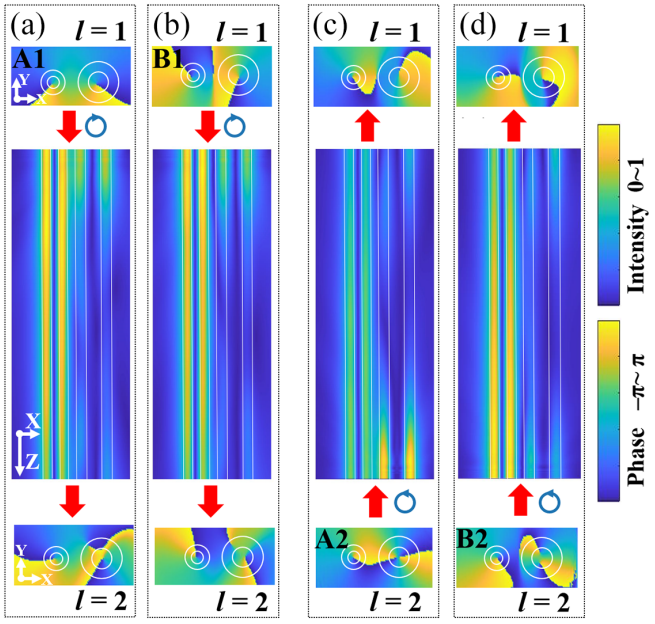

FIG. 4. Simulated OAM conversion evolution with different encircling directions and initial eigenstates. (a) CW with initial eigenstate $A1$. (b) CW with $B1$. (c) CCW with $A2$. (a) CCW with $B2$. The xy phase distributions of input and output states are shown on the top and bottom.

time, the system undergoes a NAT to ensure the field intensity mainly located in WG-2, corresponding to the state evolves on low-loss Riemann sheet that connects two spaces. When $L/2 < z < L$, state completes the final evolution in Space-2, the topological charge in WG-1 changes to $l = 2$. For Loop1 with $B1$ as the initial eigenstate [Fig. 4(b)]; topological charge in WG-1 is also $l = 1$. The state evolves on low-loss Riemann sheet from Space-1 to Space-2, and the field intensity mainly located in WG-2. Finally, the state evolves in Space-2 and the topological charge in WG-1 changes to $l = 2$. For Loop2 with eigenstate $A2$ input at $z = L$ (Fig. 4(c)), the topological charge in WG-1 is $l = 2$. As the state evolves in Space-2 ($L/2 < z < L$), it undergoes NAT to ensure that the field intensity is primarily located in WG-2, corresponding to the evolution on a low-loss Riemann sheet that connects the two spaces. When $0 < z < L/2$, state completes the final evolution in Space-1, the topological charge in WG-1 changes to $l = 1$. For Loop2 with $B2$ as the initial eigenstate [Fig. 4(d)], topological charge in WG-1 is also $l = 2$. The state evolves on low-loss Riemann sheet from Space-2 to Space-1, and the field intensity mainly located in WG-2. The state completes the final evolution in Space-1, topological charge in WG-1 changes to $l = 1$. We also verify no OAM conversion results with the same initial eigenstates but different encircling directions in Supplemental Material, Sec. III [43]. We calculate the field, the Ey field, and phase distributions at $t = 0$ and $t = T$ (illustrated in Supplemental Material, Sec. V [43]). Therefore, we demonstrate that for CW direction starting at $A1$ or $B1$, OAM in WG-1 changes from $l = 1$ to $l = 2$. For CCW direction starting at $A2$ or $B2$, OAM in WG-1 changes from $l = 2$ to $l = 1$. In the opposite direction, no conversion occurs. It is evident from the phase distribution. The process has chiral properties, and the encircling direction determines the final topological charge. For the CW loop, the topological charge changes from higher to lower. For the CCW loop, it changes from lower to higher. Our Letter is expected to be performed in experiment, and we discuss that n and k can be tuned as

TABLE. I. Our Letter compared with other works.

System	Eigenstates	Reference
Two-waveguide system	Symmetric modes	31
Waveguide system with slanted sidewall	Polarization states	32
A single nitrogen-vacancy center in diamond	Quantum states	33
Two doughnut-shaped waveguide system	OAM modes	Our Letter

required to accomplish the encircling loop in the Supplemental Material, Sec. VI [43].

Moreover, arbitrary topological charge conversion can be achieved by such EP encircling process. By constructing an encircling loop from Space-m to Space-n (where $m \neq n$; if $m < n$, the loop should be CCW, if $m > n$, the loop should be CW), we can achieve the conversion of topological charge from $l = m$ to $l = n$. It undergoes the similar aforementioned encircling process and is detailed in our theoretical analysis in Supplemental Material, Sec. VII [43].

In conclusion, we construct a non-Hermitian system comprising two doughnut-shaped waveguides, achieving OAM conversion by encircling EPs in different Riemann sheets. The conversion process is chiral, and the encircling direction determines the final topological charge. For the CW loop, the topological charge changes from higher to lower. For the CCW loop, it changes from lower to higher. Our Letter presents a special chiral behavior and provides a new method to manipulate OAM on-chip. In the future, it is expected to perform an experiment using laser direct writing [34,47] or 3D direct printing [48].

This work was supported by the National Natural Science Foundation of China under Grant No. 92150302 and the Innovation Program for Quantum Science and Technology under Grant No. 2021ZD0301500. We thank C. T. Chan at The Hong Kong University of Science and Technology for guiding this work.

*Contact author: wang_xingyuan@mail.buct.edu.cn
†Contact author: xiaoyonghu@pku.edu.cn

[1] L. Allen, M. W. Beijersbergen, R. J. C. Spreeuw, and J. P. Woerdman, Phys. Rev. A **45**, 8185 (1992).
[2] J. T. Barreiro, T. C. Wei, and P. G. Kwiat, Nat. Phys. **4**, 662 (2008).
[3] X. Y. Fang, H. R. Ren, and M. Gu, Nat. Photonics **14**, 102 (2020).
[4] H. Sroor, Y.-W. Huang, B. Sephton, D. Naidoo, A. Vallés, V. Ginis, C.-W .Qiu, A. Ambrosio, F. Capasso, and A. Forbes, Nat. Photonics **14**, 498 (2020).
[5] S. M. Chen, K. F. Li, J. H. Deng, G. X. Li, and S. Zhang, Nano Lett. **20**, 8549 (2020).
[6] R. C. Devlin, A. Ambrosio, N. A. Rubin, J. P. B. Mueller, and F. Capasso, Science **358**, 896 (2017).
[7] H. F. Zhang, M. Kang, X. Q. Zhang, W. G. Guo, C. G. Lv, Y. F. Li, W. L. Zhang, and J. G. Han, Adv. Mater. **29**, 1604252 (2017).
[8] S. N. Khonina, A. V. Ustinov, V. I. Logachev, and A. P. Porfirev, Phys. Rev. A **101**, 043829 (2020).
[9] S. J. Liu, P. Chen, S. J. Ge, L. Zhu, Y. H. Zhang, and Y. Q. Lu, Laser Photonics Rev. **16**, 2200118 (2022).
[10] B. Y. Wei, W. Hu, Y. Ming, F. Xu, S. Rubin, J. G. Wang, V. Chigrinov, and Y. Q. Lu, Adv. Mater. **26**, 1590 (2014).
[11] P. Miao, Z. F. Zhang, J. B. Sun, W. Walasik, S. Longhi, N. M. Litchinitser, and L. Feng, Science **353**, 464 (2016).
[12] Z. F. Zhang *et al.*, Science **368**, 760 (2020).
[13] W. G. Shen, Y. Chen, H. M. Wang, and X. M. Jin, Opt. Commun. **507**, 127615 (2022).
[14] F. O. Wu, Q. Zhong, H. Z. Ren, P. S. Jung, K. G. Makris, and D. N. Christodoulides, Phys. Rev. Lett. **128**, 123901 (2022).
[15] H. Hodaei, A. U. Hassan, S. Wittek, H. Garcia-Gracia, R. El-Ganainy, D. N. Christodoulides, and M. Khajavikhan, Nature (London) **548**, 187 (2017).
[16] M. A. Miri and A. Alu, Science **363**, eaar7709 (2019).
[17] S. K. Ozdemir, S. Rotter, F. Nori, and L. Yang, Nat. Mater. **18**, 783 (2019).
[18] C. Wang, W. R. Sweeney, A. D. Stone, and L. Yang, Science **373**, 1261 (2021).
[19] Q. Song, M. Odeh, J. Zuniga-Perez, B. Kante, and P. Genevet, Science **373**, 1133 (2021).
[20] A. Galda and V. M. Vinokur, Sci. Rep. **9**, 17484 (2019).
[21] X. L. Zhang, T. Jiang, and C. T. Chan, Light **8**, 88 (2019).
[22] H. Wang, S. Assawaworrarit, and S. Fan, Opt. Lett. **44**, 638 (2019).
[23] Q. Liu, S. Li, B. Wang, S. Ke, C. Qin, K. Wang, W. Liu, D. Gao, P. Berini, and P. Lu, Phys. Rev. Lett. **124**, 153903 (2020).
[24] B. Zhen, C. W. Hsu, Y. Igarashi, L. Lu, I. Kaminer, A. Pick, S. L. Chua, J. D. Joannopoulos, and M. Soljacic, Nature (London) **525**, 354 (2015).
[25] Q. Zhong, M. Khajavikhan, D. N. Christodoulides, and R. El-Ganainy, Nat. Commun. **9**, 4808 (2018).
[26] A. D. Li *et al.*, Phys. Rev. Lett. **125**, 187403 (2020).
[27] X. L. Zhang and C. T. Chan, Commun. Phys. **2**, 63 (2019).
[28] J. W. Yoon *et al.*, Nature (London) **562**, 86 (2018).
[29] H. K. Gandhi, A. Laha, S. Dey, and S. Ghosh, Opt. Lett. **45**, 1439 (2020).
[30] X. L. Zhang, S. B. Wang, B. Hou, and C. T. Chan, Phys. Rev. X **8**, 021066 (2018).
[31] J. Doppler *et al.*, Nature (London) **537**, 76 (2016).
[32] A. U. Hassan, B. Zhen, M. Soljacic, M. Khajavikhan, and D. N. Christodoulides, Phys. Rev. Lett. **118**, 093002 (2017).
[33] W. Q. Liu *et al.*, Phys. Rev. Lett. **126**, 201102 (2021).
[34] Y. Chen, J. Gao, Z. Q. Jiao, K. Sun, W. G. Shen, L. F. Qiao, H. Tang, X. F. Lin, and X. M. Jin, Phys. Rev. Lett. **121**, 233602 (2018).
[35] L. Fang and J. Wang, Phys. Rev. Lett. **127**, 233902 (2021).
[36] Y. Chen *et al.*, Phys. Rev. Lett. **124**, 153601 (2020).
[37] C. Liu *et al.*, Optica **7**, 192 (2020).
[38] S. Piacentini, T. Vogl, G. Corrielli, P. K. Lam, and R. Osellame, Laser Photonics Rev. **15**, 2000167 (2021).
[39] P. Z. Dashti, F. Alhassen, and H. P. Lee, Phys. Rev. Lett. **96**, 043604 (2006).
[40] A. Hardy, S. Shakir, and W. Streifer, Opt. Lett. **11**, 324 (1986).
[41] H. Renner, Opt. Quantum Electron. **24**, 647 (1992).
[42] G. L. Yin, C. C. Liang, I. P. Ikechukwu, M. Deng, L. L. Shi, Q. J. Fu, T. Zhu, and L. Zhang, Opt. Lett. **44**, 999 (2019).
[43] See Supplemental Material at http://link.aps.org/supplemental/10.1103/PhysRevLett.132.243802 for mathematical derivations, no topological charge conversion process, arbitrary topological charge conversion process

and additional figures. It includes Refs. [19,21,23,26,27,30–34,36–38,42].
[44] X. Zhu, A. Schulzgen, H. Li, H. Wei, J. V. Moloney, and N. Peyghambarian, Opt. Express **18**, 7506 (2010).
[45] B. W. Mao, Y. G. Liu, H. W. Zhang, K. Yang, Y. Han, Z. Wang, and Z. H. Li, Nanophotonics **8**, 271 (2019).
[46] G. Liang, Y. Q. Wang, Q. Guo, and H. C. Zhang, Opt. Express **26**, 8084 (2018).
[47] K. Weber, F. Hutt, S. Thiele, T. Gissibl, A. Herkommer, and H. Giessen, Opt. Express **25**, 19672 (2017).
[48] S. Lightman, O. Porat, G. Hurvitz, and R. Gvishi, Opt. Lett. **47**, 5248 (2022).